Nur'ainul Miftahul Huda

Manuscript Cauchy.pdf

Paper 4
FMIPA Oke
Universitas Tanjungpura

Document Details

Submission ID
trn:oid:::1:3601305213

Submission Date
Jun 25, 2026, 1:12 PM GMT+7

Download Date
Jun 25, 2026, 1:15 PM GMT+7

File Name
Manuscript_Cauchy.pdf

File Size
18.3 MB

16 Pages

7,162 Words

41,789 Characters

9% Overall Similarity

The combined total of all matches, including overlapping sources, for each database.

Filtered from the Report

- Bibliography
- Quoted Text

Match Groups

44 Not Cited or Quoted 9%
Matches with neither in-text citation nor quotation marks

0 Missing Quotations 0%
Matches that are still very similar to source material

0 Missing Citation 0%
Matches that have quotation marks, but no in-text citation

0 Cited and Quoted 0%
Matches with in-text citation present, but no quotation marks

Top Sources

7% Internet sources
6% Publications
4% Submitted works (Student Papers)

Match Groups

- **44** Not Cited or Quoted 9%
  Matches with neither in-text citation nor quotation marks
- **0** Missing Quotations 0%
  Matches that are still very similar to source material
- **0** Missing Citation 0%
  Matches that have quotation marks, but no in-text citation
- **0** Cited and Quoted 0%
  Matches with in-text citation present, but no quotation marks

Top Sources

7% Internet sources
6% Publications
4% Submitted works (Student Papers)

Top Sources

The sources with the highest number of matches within the submission. Overlapping sources will not be displayed.

1	Internet	ejournal.uin-malang.ac.id 3%
2	Internet	ceur-ws.org <1%
3	Publication	Yohanes Setiawan, Regita Putri Permata, Adzanil Rachmadi Putra, Cisa Valentino ... <1%
4	Publication	Nur'ainul Miftahul Huda, Nurfitri Imro'ah. "Covid-19 case modeling in Java Island ... <1%
5	Internet	cbio.ensmp.fr <1%
6	Internet	journal.ummat.ac.id <1%
7	Student papers	Strathmore University (Main Account) <1%
8	Publication	Pu Wang, Zhihong Feng, Yan Tang, Yuzhi Zhang. "A Fingerprint Database Reconst... <1%
9	Publication	Takvor Soukissian, Vasilis Apostolou. "The Effects of Offshore Wind Interpolation ... <1%
10	Student papers	Chiang Mai University <1%

11	Publication	
Juan Wang, Tingting Shi, Hui Wang, Meng Li, Xiaobo Zhang, Luqi Huang. "Estimati...		<1%
12	Publication	
Resti Arsanti, Neva Satyahadewi, Shantika Martha. "Forecasting the Stock Price o...		<1%
13	Student papers	
University of Nottingham		<1%
14	Internet	
d197for5662m48.cloudfront.net		<1%
15	Internet	
mpra.ub.uni-muenchen.de		<1%
16	Internet	
stax.strath.ac.uk		<1%
17	Internet	
www.cs.cornell.edu		<1%
18	Internet	
revista.domhelder.edu.br		<1%
19	Internet	
www.mdpi.com		<1%
20	Internet	
www.research-collection.ethz.ch		<1%
21	Publication	
Christian M Mulomba, Vogel M Kiketa, David M Kutangila, Pescie H K Mampuya et...		<1%
22	Publication	
Saheed Ajobo, Oluwayemisi O. Alaba, Ahmad Zaenal. "Generalised Space-Time Se...		<1%
23	Internet	
smartsatcrc.lbcdn.io		<1%
24	Internet	
www.econstor.eu		<1%

turnitin Page 5 of 20 - Integrity Submission Submission ID trn:oid:::1:3601305213

CAUCHY – Jurnal Matematika Murni dan Aplikasi
Volume 11 (2) (2026), Pages 1-16
p-ISSN: 2086-0382; e-ISSN: 2477-3344

Continuous Spatial Reconstruction of Grid-Based FRP Forecasts using Ordinary Kriging and GSTARX-IDW Models

Nurfitri Imro'ah[1*], Nur'ainul Miftahul Huda[2], Yundari[2], and Gita Fitriyana[1]

[1]*Department of Statistics, Universitas Tanjungpura, Pontianak, Indonesia*
[2]*Department of Mathematics, Universitas Tanjungpura, Pontianak, Indonesia*

Abstract

The study presents a combined spatio-temporal forecasting framework using the Generalised Space-Time Autoregressive with Exogenous Variables (GSTARX-IDW) model and Ordinary Kriging to map the weekly Fire Radiative Power (FRP) dynamics in West Kalimantan from January 2021 to September 2025. We find a strong dominance of spatial contagion in the estimation of parameters, with the spatial autoregressive parameter (β_{p1}) being statistically significant in 95.56% of operational grids, providing empirical validation of Tobler's First Law of Geography. Locally, land surface temperature is an important forcing variable, showing geographic dichotomies driven by deep peatland drying cycles. The residual diagnostics show a 100% deviation from Gaussian normality, due to sudden stochastic fire bursts. This unstructured noise is successfully handled by the addition ofOrdinary Kriging as a secondary refinement step, resulting in fluid prediction surfaces for October 2025. The hybrid system can obtain an excellent modelling accuracy with a Root Mean Squared Error (RMSE) of 1.1380, a Mean Absolute Error (MAE) of 0.8736, a Mean Absolute Percentage Error (MAPE) of 18.5873%, and a stable Mean Absolute Scaled Error (MASE) of 1.0008. This strong framework provides a mathematically robust computational baseline for real-time multi-disaster prediction networks in the highly fragmented tropical landscapes.

Keywords: Land surface temperature; Peatland ecosystems; Space-time diagnostics; Wildfire dynamics.

Copyright © 2026 by Authors, Published by CAUCHY Group. This is an open access article under the CC BY-SA License (https://creativecommons.org/licenses/by-sa/4.0)

1. Introduction

Modeling data with spatial and temporal dependence is one of the most challenging problems in modern statistical analysis [1], [2]. Traditional time series methods often ignore spatial interactions, and purely spatial models tend to ignore temporal dynamics. The Generalized Space-Time Autoregressive (GSTAR) model is a powerful framework for capturing concurrent space-time evolution across multiple locations and overcomes the limitations of the above models [3], [4]. The inclusion of exogenous variables, relevant environmental driving forces, can considerably improve the classical GSTAR model, resulting in the GSTARX framework [5].

In addition to selecting a suitable model structure, the precision of spatio-temporal forecasting is strongly influenced by the representation of spatial units [6]. In traditional spatio-temporal analyses of environmental data, the data are usually aggregated based on administrative boundaries

*Corresponding author. E-mail: nurfitriimroah@math.untan.ac.id

Submitted: ... Reviewed: ... Accepted: ...
DOI: https://doi.org/10.18860/cauchy.v11i2.32446

turnitin Page 5 of 20 - Integrity Submission Submission ID trn:oid:::1:3601305213

(e.g., regencies or districts). However, this approach suffers from severe statistical biases, such as the Modifiable Areal Unit Problem (MAUP), in which the arbitrary shapes and heterogeneous sizes of political zones obscure the characteristics of spatial autocorrelation [7]. To overcome these limitations, this study moves away from arbitrary administrative boundaries and uses a regular grid with a 0.5×0.5 degree resolution. This grid topology ensures that all observational units are spatially homogeneous and fixes the physical distance between neighboring grid centroids to approximately 55.5 kilometres, allowing the model to capture the objective physical diffusion of phenomena without administrative distortion.

In the GSTARX framework, the definition of the spatial weight matrix plays a critical role because it represents the spatial interaction patterns of the observed locations in a mathematical form [8]. Binary contiguity matrices (e.g. Queen or Rook specifications) are widely used in classic spatial modelling where only shared boundaries are considered and all neighbours are treated equally regardless of distance [9]. Such binary settings are not enough to model continuous physical diffusion processes. Therefore, in this work we use an Inverse Distance Weighting (IDW) matrix based on the distance-decay principle, where the spatial weight between grid centroids monotonically decreases with increasing physical distance . This formulation is consistent with the physical mechanics of spatial contagion and realistic parameter estimation requirements.

However, the use of a grid-based framework for large-scale environmental phenomena can impose severe mathematical constraints such as matrix singularity. In many grid cells the target variable may be completely inactive or have zero variance in the whole observation period. In terms of estimation, the presence of these inactive units in the optimisation protocols (e.g., ordinary least squares, or seemingly unrelated regressions) simultaneously produces a singular covariance matrix that cannot be inverted. Before model estimation, a rigorous grid filtering technique is necessary to remove passive grid cells and to direct the predictive engine only to the functionally active zones, to ensure numerical stability and the statistical validity of the parameter estimates.

Such a comprehensive spatio-temporal framework is well-suited to addressing critical environmental disasters, such as recurring large-scale forest fires in West Kalimantan, Indonesia. One of the most vulnerable provinces during the prolonged dry season, this region experiences aggressive biomass burning that emits large volumes of greenhouse gases and particulate matter, resulting in catastrophic transboundary haze and severe ecosystem degradation [10], [11], [12]. To achieve continuous and accurate monitoring, this study adopts the Fire Radiative Power (FRP) metric, which quantifies the radiant energy emitted by active flames and is derived from MODIS and VIIRS satellite sensors via NASA's FIRMS platform. FRP provides a much more robust measure of fire intensity and biomass consumption rates than simply counting hotspots [13], [14], [15]. The proposed grid-based GSTARX-IDW framework aims to provide a structurally rigorous and precise predictive system for wildfire risk management and emergency response optimization in West Kalimantan, using land surface temperature as an exogenous variable that reflects vegetation flammability and fuel dryness.

2. Methods

This research introduces a comprehensive spatiotemporal computational framework that combines Generalized Space-Time Autoregressive with Exogenous Variable (GSTARX) modeling and Ordinary Kriging geostatistical refinement to examine and forecast Fire Radiative Power (FRP) dynamics in West Kalimantan. Figure 1 illustrates the whole operational architecture of this methodology to give a complete view of the systematic implementation, data filtering protocols, diagnostic decision nodes, and the final surface projection mapping.

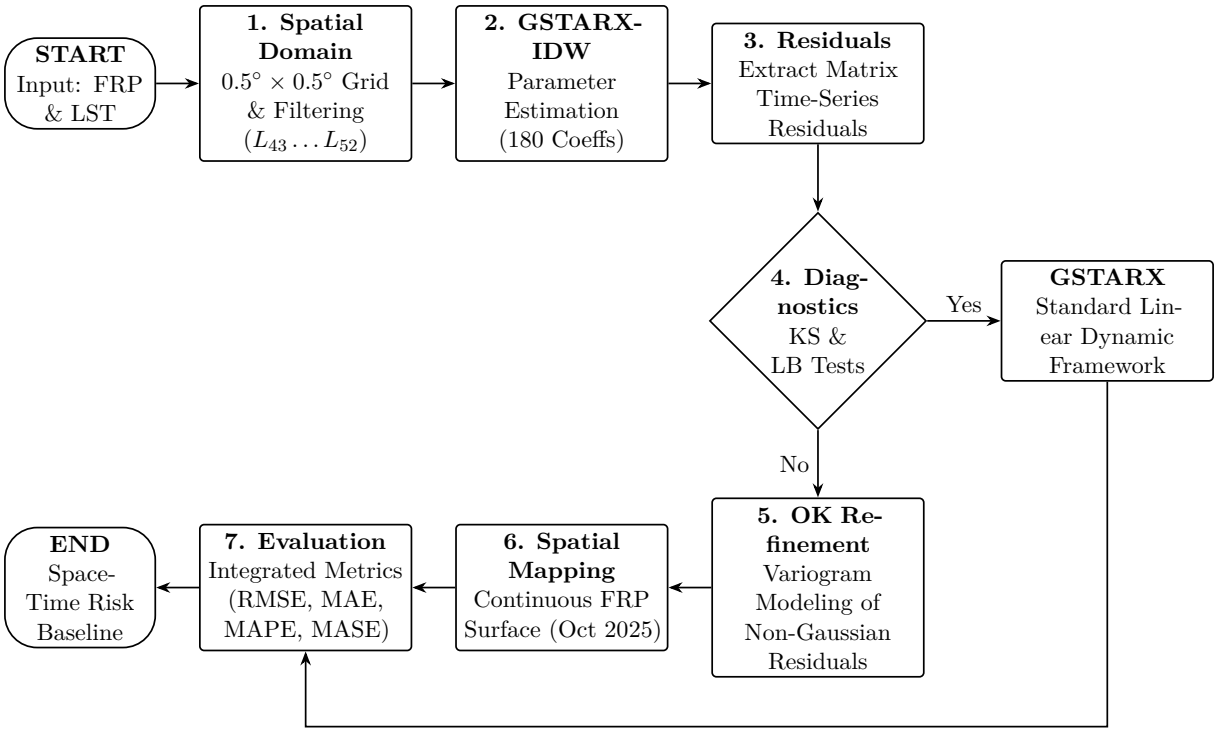

Fig. 1: Flowchart of the integrated GSTARX-IDW and Ordinary Kriging framework

2.1. Generalized Space-Time Autoregressive with Exogenous Variable (GSTARX) Modeling

The Generalized Space-Time Autoregressive with exogenous variable (GSTARX($p;q$)) framework model is employed to jointly characterize temporal dependencies, spatial interactions, and external systemic influences within a unified system [4], [16]. To maintain the structural consistency of generalized spatial units, the model is formulated in compact matrix-vector notation. Let $\mathbf{Y}_t = [Y_1(t), Y_2(t), \dots, Y_n(t)]^T$ be the $(n \times 1)$ vector of the endogenous target variable observed over n spatial grid cells at week t. At the same time, denote by $\mathbf{X}_t = [X_1(t), X_2(t), \dots, X_n(t)]^T$ the corresponding $(n \times 1)$ vector of the localised exogenous covariate. The general mathematical framework of the GSTARX($p;q$) process is presented as follows [5]:

$$\mathbf{Y}_t = \sum_{k=1}^{p} (\mathbf{\Phi}_{k0}\mathbf{Y}_{t-k} + \mathbf{\Phi}_{k1}\mathbf{W}\mathbf{Y}_{t-k}) + \sum_{m=1}^{q} (\mathbf{\Gamma}_{m0}\mathbf{X}_{t-m} + \mathbf{\Gamma}_{m1}\mathbf{W}\mathbf{X}_{t-m}) + \mathbf{e}_t \tag{1}$$

In Equation (1) p and q denote the maximum temporal lag orders for the endogenous and exogenous processes, respectively. The $(n \times n)$ parameter matrices $\mathbf{\Phi}_{k0}$ and $\mathbf{\Phi}_{k1}$ characterise the localised temporal autoregressive effects and the spatio-temporal autoregressive coefficients for lag k, respectively, which govern the dynamic internal relationships within the spatial system. Simultaneously, the effects of external forcing are modelled through the $(n \times n)$ parameter matrices $\mathbf{\Gamma}_{m0}$ and $\mathbf{\Gamma}_{m1}$, which describe the local exogenous impact and the spatio-exogenous cross-dependencies for lag m, respectively. The $(n \times n)$ spatial interaction weight matrix $\mathbf{W}$ explicitly accounts for the spatial connectivity among the network. The unresolved structural variation is absorbed by $\mathbf{e}_t = [e_1(t), e_2(t), \dots, e_n(t)]^T$, the $(n \times 1)$ vector of localised idiosyncratic error terms assumed to follow a white noise process with expectation $\mathbb{E}[\mathbf{e}_t] = \mathbf{0}$.

The generalized nature of this framework is explicitly governed by the diagonal structure of the parameter matrices. For any given lag, the parameter configurations are defined as $\mathbf{\Phi}_{k0} = \text{diag}(\phi_{k0}^{(1)}, \phi_{k0}^{(2)}, \dots, \phi_{k0}^{(n)})$ and $\mathbf{\Gamma}_{m0} = \text{diag}(\gamma_{m0}^{(1)}, \gamma_{m0}^{(2)}, \dots, \gamma_{m0}^{(n)})$, thereby mathematically guaranteeing that each unique functional grid cell retains its specific, highly localized parameter features.

The spatial weight matrix $\mathbf{W}$ is constructed through Inverse Distance Weighting (IDW) to capture the effects of geographic distance decay in the spatial grid system. The spatial centroids of grid i and grid j are spatially separated by the following standard Euclidean metric [17]:

$$d_{ij} = \sqrt{(x_i - x_j)^2 + (y_i - y_j)^2} \tag{2}$$

where (x, y) represents the explicit geographic longitude and latitude coordinates of the respective grid centers. The unnormalized interaction components w_{ij}^* are subsequently defined as [18]:

$$w_{ij}^* = \begin{cases} \frac{1}{d_{ij}^{\alpha}}, & \text{if } i \neq j \\ 0, & \text{if } i = j \end{cases} \tag{3}$$

where α is the distance friction parameter. Here, the exponent is fixed to $\alpha = 1$, corresponding to the standard linear geographic decay of spatial influence. Moreover, a global neighborhood structure is assumed, i.e., spatial interactions are calculated across all active grid units in the study area without imposing an artificial distance cutoff. To satisfy the statistical equilibrium and structural stability conditions of space-time modeling, a strict row-normalization scaling is imposed [19]:

$$w_{ij} = \frac{w_{ij}^*}{\sum_{j=1}^{n} w_{ij}^*} \tag{4}$$

Such a normalization constraint leads to $\sum_{j=1}^{n} w_{ij} = 1$ for the row operations in the matrix, which ensures that the spatial lag terms $\mathbf{WY}_{t-k}$ and $\mathbf{WX}_{t-m}$ well scale the regional weighted average of neighboring intensities. Figure 2 provides a systematic representation of the conceptualization of this distance-decay mechanism and the subsequent distribution of spatial weights among neighboring observation units.

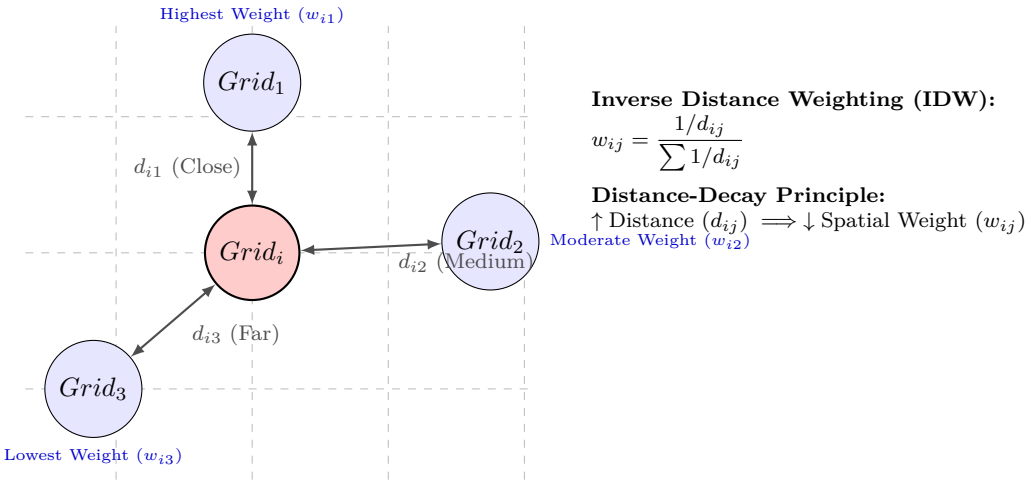

Fig. 2: Conceptual illustration of the standard Inverse Distance Weighting (IDW) spatial interaction structure among regular grid centroids based on the distance-decay principle.

2.2. Ordinary Kriging for Spatial Prediction Mapping

The GSTARX framework produces point forecast of a spatio-temporal variable at the centroids of the observed spatial units. These predictions produce localized temporal trajectories at each specific location, but do not generate the continuous spatial risk surface across unobserved geographic locations between the sample points [20]. To overcome this limitation and to reconstruct a continuous spatial distribution of forecasted intensities for a future horizon, Ordinary Kriging OK is applied directly over the forecasted point estimates.

Let $\hat{Y}(\mathbf{s}_0; t+k)$ be the unknown forecasted value at an unsampled spatial coordinate $\mathbf{s}_0$ for a future lead time $t+k$ ($k \geq 1$). The continuous spatial predictor in Ordinary Kriging is related to a linear combination of the forecasted values given by the GSTARX model at the n surrounding observed spatial centroids [21]:

$$\hat{Y}(\mathbf{s}_0; t+k) = \sum_{i=1}^{n} \lambda_i \hat{Y}(\mathbf{s}_i; t+k) \tag{5}$$

where $\hat{Y}(\mathbf{s}_i; t+k)$ is the k-step ahead point forecast from the GSTARX model at the i-th spatial centroid and λ_i is the spatial weight associated with the localized forecast.

To guarantee that the continuous spatial surface estimator is the Best Linear Unbiased Predictor (BLUP), Ordinary Kriging imposes the unbiasedness constraint, requiring the sum of the spatial weights equal to unity [22]:

$$\sum_{i=1}^{n} \lambda_i = 1 \tag{6}$$

The weights λ_i are then optimized to minimize the estimation variance, $\mathrm{Var}\left(\hat{Y}(\mathbf{s}_0; t+k) - Y(\mathbf{s}_0; t+k)\right)$, under this constraint. The system of Ordinary Kriging equations is formulated using the Lagrange multiplier (μ) optimization technique as follows [23]:

$$\sum_{j=1}^{n} \lambda_j \gamma(\mathbf{s}_i, \mathbf{s}_j) + \mu = \gamma(\mathbf{s}_i, \mathbf{s}_0), \quad \forall i = 1, \ldots, n \tag{7}$$

where $\gamma(\mathbf{s}_i, \mathbf{s}_j)$ is the spatial semivariance between the observed centroids $\mathbf{s}_i$ and $\mathbf{s}_j$.

The spatial continuity of the predicted field is described by an experimental semivariogram $\gamma(\mathbf{h})$, computed from the spatial variability of the point predictions [24]:

$$\gamma(\mathbf{h}) = \frac{1}{2N(\mathbf{h})} \sum_{i=1}^{N(\mathbf{h})} \left[\hat{Y}(\mathbf{s}_i; t+k) - \hat{Y}(\mathbf{s}_i + \mathbf{h}; t+k)\right]^2 \tag{8}$$

where $\mathbf{h}$ is the lag distance separating the spatial centroids, this experimental semivariogram is fitted to theoretical mathematical models (e.g., Spherical, Exponential, and Gaussian) to ensure a positive-definite Kriging system, which guarantees mathematically valid interpolation maps over the entire continuous spatial domain [22].

Specifically, the three candidate theoretical semivariogram models $\gamma(\mathbf{h})$ evaluated in this framework are detailed below [25]:

1. **Exponential Model:** Describes a spatial continuity that increases linearly near the origin but approaches the sill asymptotically:

$$\gamma(\mathbf{h}) = \begin{cases} 0, & \text{if } |\mathbf{h}| = 0 \\ C_0 + C\left[1 - \exp\left(-\frac{|\mathbf{h}|}{a}\right)\right], & \text{if } |\mathbf{h}| > 0 \end{cases}$$

2. **Spherical Model:** Represents a highly localized spatial structure that strictly reaches its bounded sill at the finite range distance a:

$$\gamma(\mathbf{h}) = \begin{cases} 0, & \text{if } |\mathbf{h}| = 0 \\ C_0 + C\left[\frac{3}{2}\left(\frac{|\mathbf{h}|}{a}\right) - \frac{1}{2}\left(\frac{|\mathbf{h}|}{a}\right)^3\right], & \text{if } 0 < |\mathbf{h}| \leq a \\ C_0 + C, & \text{if } |\mathbf{h}| > a \end{cases}$$

3. **Gaussian Model:** Models an extremely smooth, parabolic spatial continuity near the geographic origin:

$$\gamma(\mathbf{h}) = \begin{cases} 0, & \text{if } |\mathbf{h}| = 0 \\ C_0 + C\left[1 - \exp\left(-\frac{|\mathbf{h}|^2}{a^2}\right)\right], & \text{if } |\mathbf{h}| > 0 \end{cases}$$

where C_0 denotes the nugget effect, C represents the partial sill, and a signifies the spatial range parameter.

2.3. Model Evaluation and Validation Metrics

Objective statistical indices are used to rigorously assess the goodness-of-fit and modeling accuracy of the integrated spatio-temporal framework, which combines discrete GSTARX-IDW grid outputs with continuous Ordinary Kriging residual refinement. The validation procedure does not assess the temporal and spatial phases separately, but rather the overall modeling ability of the combined hybrid system in reproducing the observed FRP bursts over the operational spatial network during the estimation period.

The global difference between the observed empirical values and the fitted values from the integrated framework is assessed using four complementary error metrics: Root Mean Squared Error (RMSE), Mean Absolute Error (MAE), Mean Absolute Percentage Error (MAPE), and Mean Absolute Scaled Error (MASE). Let $Y_i(t)$ be the actual empirical observation for spatial unit i at time t, and $\hat{Y}_i(t)$ be the corresponding fitted value from the combined GSTARX-Kriging model. The global metrics are defined over an estimation horizon of T periods and n functional grid locations as follows [26]:

$$\text{RMSE} = \sqrt{\frac{1}{n \cdot T} \sum_{i=1}^{n} \sum_{t=1}^{T} \left(Y_i(t) - \hat{Y}_i(t)\right)^2} \tag{9}$$

$$\text{MAE} = \frac{1}{n \cdot T} \sum_{i=1}^{n} \sum_{t=1}^{T} \left|Y_i(t) - \hat{Y}_i(t)\right| \tag{10}$$

To capture the proportional scale of the modeling residuals relative to the actual fire intensities, the global Mean Absolute Percentage Error (MAPE) is incorporated and defined as [27]:

$$\text{MAPE} = \frac{100\%}{n \cdot T} \sum_{i=1}^{n} \sum_{t=1}^{T} \left|\frac{Y_i(t) - \hat{Y}_i(t)}{Y_i(t)}\right| \tag{11}$$

Furthermore, the Mean Absolute Scaled Error (MASE) is calculated as a scale-independent benchmark that is robust to local variances. The global MASE is obtained by dividing the absolute estimation errors of the hybrid framework by the baseline performance of one in-sample one-step-ahead historical non-seasonal naive framework as [28]:

$$\text{MASE} = \frac{\text{MAE}}{\frac{1}{n(T-1)} \sum_{i=1}^{n} \sum_{t=2}^{T} |Y_i(t) - Y_i(t-1)|} \tag{12}$$

Mathematically, a global MASE value close to or less than unity indicates that the proposed integrated space-time hybrid framework systematically outperforms a baseline historical naive model, demonstrating that the geostatistical refinement phase successfully isolates and absorbs the underlying structural noise during model estimation.

3. Result and Discussion

3.1. Spatial Domain Definition and Data Filtering

The spatial domain of the study area must be clearly defined before applying the spatio-temporal modeling framework. Figure 3 is the West Kalimantan research area map. The map is divided into a system of regular grids to conceptualize the spatial interaction unit . The spatial resolution is described by the grid size of $0.5° \times 0.5°$, and the physical distance between the centroid of neighbouring grid cells is about 55.5 km. This specific resolution is selected so as to be able to record localized atmospheric and environmental variations without sacrificing spatial continuity. The period of observation is from January 2021 to September 2025 with weekly temporal resolution. The spatial domain initially consists of several grid blocks that cover the

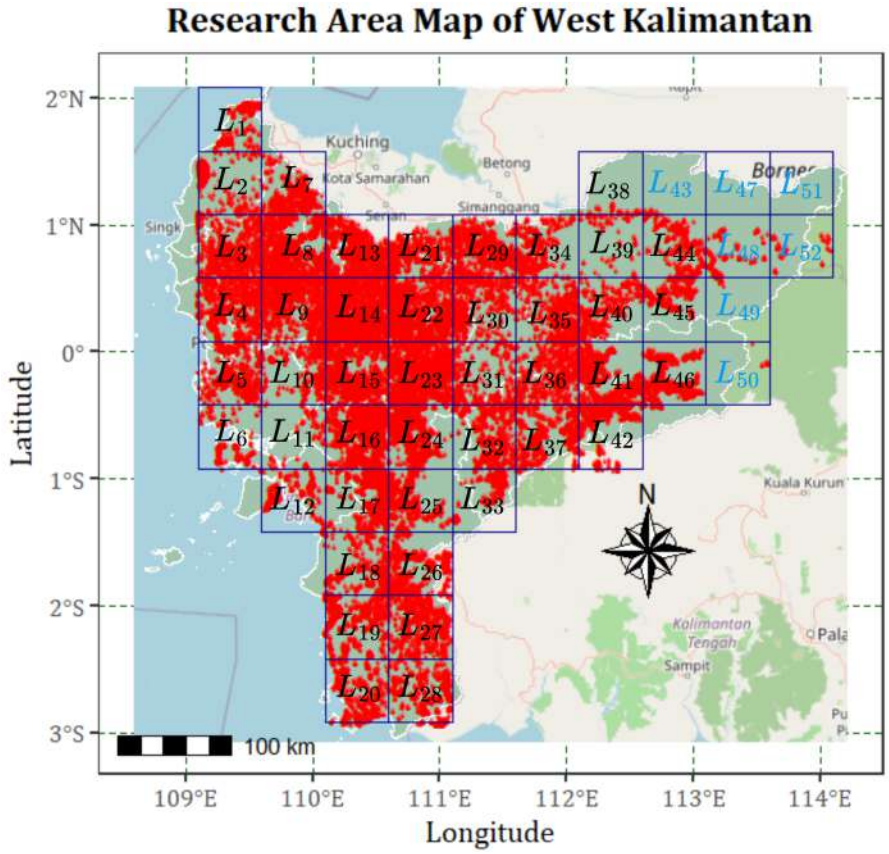

Fig. 3: Research area map of West Kalimantan partitioned into regular grid systems

entire province, as shown in Figure 3. However, a thorough data filtering process was employed to ensure the statistical robustness of the GSTARX-IDW model. The blue highlighted grid labels, L_{43}, L_{47}, L_{48}, L_{49}, L_{50}, L_{51} and L_{52}, refer to the specific regions that have been excluded from the subsequent analysis and model estimation by design.

The exclusion of these seven grid cells is justified epidemiologically and statistically by the nature of the target variable. These coordinates had mostly zero Fire Radiative Power (FRP) values during the observed period from January 2021 to September 2025, indicating a substantial dearth of significant or extended wildfire events during those weeks. In spatial statistics, forcing a high zero-inflation density into a continuous linear dynamic model such as GSTARX can result in severe bias in the parameter estimates, singularity errors in the inversion of the weight matrix, and a distorted variance structure. Hence, the final modeling framework is limited to the remaining 45 active functional grid cells to ensure that the estimated spatial weights and exogenous coefficients are representative of the actual, non-trivial dynamics of weekly wildfire intensities across West Kalimantan.

3.2. GSTARX-IDW Parameter Estimation and Spatial Contagion

The empirical results of the parameter estimation for the GSTARX-IDW model across the 45 functional grid cells are summarized in Table 1.

Table 1: Summary of parameter significance for the GSTARX-IDW model

Par.	Type	Total	Signif. Count	Non-Signif. Count	% Signif.
β_{p0}	Temporal Effect (Y_{t-1})	45	24	21	53.33%
β_{p1}	Spatial Effect (WY_{t-1})	45	43	2	95.56%
γ_{p0}	Exogenous Effect (X_t)	45	6	39	13.33%
γ_{p1}	Spatio-Exogenous Effect (WX_t)	45	5	40	11.11%
Total		**180**	**78**	**102**	**43.33%**

Table 2: Parameter estimates for grid locations exhibiting significant exogenous temperature effects

Grid	Parameter	Type	Estimate	Std. Error	t-Stat	p-value
L1	$\gamma_{1,0}$	Local Exogenous (X_t)	14.351	4.287	3.348	0.001*
	$\gamma_{1,1}$	Spatio-Exogenous (WX_t)	-13.956	4.200	-3.323	0.001*
L4	$\gamma_{4,0}$	Local Exogenous (X_t)	11.647	5.929	1.965	0.049*
	$\gamma_{4,1}$	Spatio-Exogenous (WX_t)	-11.124	5.844	-1.904	0.057
L7	$\gamma_{7,0}$	Local Exogenous (X_t)	12.481	3.306	3.775	0.000*
	$\gamma_{7,1}$	Spatio-Exogenous (WX_t)	-12.348	3.302	-3.739	0.000*
L34	$\gamma_{34,0}$	Local Exogenous (X_t)	-17.069	5.844	-2.921	0.003*
	$\gamma_{34,1}$	Spatio-Exogenous (WX_t)	17.246	5.891	2.928	0.003*
L36	$\gamma_{36,0}$	Local Exogenous (X_t)	-15.820	6.553	-2.414	0.016*
	$\gamma_{36,1}$	Spatio-Exogenous (WX_t)	16.145	6.599	-2.447	0.014*
L42	$\gamma_{42,0}$	Local Exogenous (X_t)	12.556	4.980	2.521	0.012*
	$\gamma_{42,1}$	Spatio-Exogenous (WX_t)	-12.470	4.948	-2.520	0.012*

By substituting the operational lag structures ($p = 1$ for temporal states and $q = 0$ for contemporary exogenous triggers) into the general framework, the estimated global spatio-temporal GSTARX process is expressed in the following matrix notation:

$$\hat{\mathbf{Y}}_t = \hat{\mathbf{\Phi}}_{10}\mathbf{Y}_{t-1} + \hat{\mathbf{\Phi}}_{11}\mathbf{W}\mathbf{Y}_{t-1} + \hat{\mathbf{\Gamma}}_{00}\mathbf{X}_t + \hat{\mathbf{\Gamma}}_{01}\mathbf{W}\mathbf{X}_t \tag{13}$$

where $\hat{\mathbf{\Phi}}_{10} = \text{diag}(\hat{\beta}_{1,0}, \ldots, \hat{\beta}_{45,0})$, $\hat{\mathbf{\Phi}}_{11} = \text{diag}(\hat{\beta}_{1,1}, \ldots, \hat{\beta}_{45,1})$, $\hat{\mathbf{\Gamma}}_{00} = \text{diag}(\hat{\gamma}_{1,0}, \ldots, \hat{\gamma}_{45,0})$, and $\hat{\mathbf{\Gamma}}_{01} = \text{diag}(\hat{\gamma}_{1,1}, \ldots, \hat{\gamma}_{45,1})$ represent the 45×45 diagonal parameter matrices estimated via the IDW spatial weight configuration $\mathbf{W}$.

To illustrate the explicit localized algebraic mechanisms generated by this matrix system, the estimated equations for Grid L1 and Grid L34 are extracted directly from the diagonal elements as follows:

$$\hat{Y}_{1,t} = \hat{\beta}_{1,0}Y_{1,t-1} + \hat{\beta}_{1,1}\sum_{j=1}^{45} w_{1j}Y_{j,t-1} + 14.351X_{1,t} - 13.956\sum_{j=1}^{45} w_{1j}X_{j,t} \tag{14}$$

$$\hat{Y}_{34,t} = \hat{\beta}_{34,0}Y_{34,t-1} + \hat{\beta}_{34,1}\sum_{j=1}^{45} w_{34j}Y_{j,t-1} - 17.069X_{34,t} + 17.246\sum_{j=1}^{45} w_{34j}X_{j,t} \tag{15}$$

where w_{ij} denotes the localized entry of the standardized spatial weight matrix $\mathbf{W}$.

The empirical results presented in Table 1 reveal crucial insights into the macro-level dynamics of weekly Fire Radiative Power (FRP) modeling using the GSTARX-IDW framework. A profound

finding is the absolute dominance of the spatial autoregressive parameter (β_{p1}), which achieves statistical significance in 43 out of 45 functional grid cells (95.56%). This widespread significance strongly confirms the existence of tight weekly spatial dependency across West Kalimantan's wildfire distribution.

It empirically validates Tobler's First Law of Geography within this context, proving that fire intensity in a specific grid cell during a given week is critically accelerated by the burning intensity of its physical neighbors in the preceding week ($t-1$). Furthermore, this structural success provides a solid mathematical justification for utilizing the Inverse Distance Weighting (IDW) spatial weight matrix, demonstrating its capacity to properly model the continuous decay of physical distance influences over weekly intervals.

In contrast, the local temporal effect (β_{p0}) exhibits a moderate influence, remaining significant in 53.33% of the grid locations. This implies that while contemporary weekly fire intensities are partially driven by their own historical footprints from the previous week, spatial interactions among neighboring clusters act as a more critical catalyst in the propagation and expansion of hotspots over time.

A notable architectural behavior of the GSTARX model is reflected in the low global significance of the weekly exogenous parameters, where the local temperature (γ_{p0}) and spatio-exogenous temperature (γ_{p1}) only account for 13.33% and 11.11% of the grids, respectively. From a statistical perspective, this minor linear coverage does not signify a failure of the exogenous covariates; rather, it indicates that weekly aggregated land surface temperature shares a highly localized or non-linear relationship with sudden, intense spikes of FRP. Since wildfire ignition often relies on critical biophysical thresholds rather than a continuous weekly linear progression, standard linear parameters at the same temporal lag cannot fully capture the overarching thermal dynamics.

This micro-structural divergence can be further contextualized by the unique edaphic and ecological profiles of West Kalimantan, which is characterized by extensive tropical peatland ecosystems. Peat fires are notoriously driven by subsurface smoldering dynamics rather than open, rapid atmospheric combustion. Once ignition occurs, the fire propagates laterally through deep organic soil layers toward adjacent zones, causing a powerful spatial contagion effect that explains the near-absolute significance (95.56%) of the spatial lag component ($\mathbf{WY}_{t-k}$). Because these underground fires can persist independently of weekly atmospheric shifts, contemporary fluctuations in land surface temperature ($\mathbf{X}_t$) exhibit a weaker linear grip on active fire intensities across the majority of the grid framework.

Looking at the aggregated estimation landscape, the systemic non-significance of the exogenous blocks directly pulls down the overall model parameter significance rate to 43.33% (78 out of 180 parameters). This overall baseline architecture implies that while the GSTARX-IDW framework excels at capturing spatial contagion and directional diffusion patterns, a standard linear integration of exogenous meteorological covariates introduces high structural sparsity into the system. Consequently, these findings suggest that future iterations of space-time wildfire modeling should pivot toward incorporating non-linear threshold parameters, such as Threshold-GSTARX architectures, or utilizing complex physical drought indices (e.g., the Keetch-Byram Drought Index) instead of raw temperature values to better map the highly localized, non-linear triggers of extreme Fire Radiative Power events.

To dissect these highly localized environmental relationships, Table 2 isolates the specific functional grid cells where weekly temperature constraints break through the global threshold. In these localized clusters (L1, L4, L7, L34, L36, and L42), weekly land surface temperature acts as a critical forcing variable. An interesting spatial dichotomy is observed in the parameter signs:

1. **Symmetric Coupled Sign (L1, L7, and L42):** The local exogenous coefficient (γ_{p0}) is positive while the spatio-exogenous coefficient (γ_{p1}) is negative. This pattern suggests an immediate cumulative thermal triggering effect within the grid cell itself during that week, whereas elevated weekly temperatures in neighboring grids concurrently create a

suppressing or stabilizing effect, potentially due to distinct local canopy moisture features or shifting regional wind vector fields.

2. **Reversed Polarity Sign (L34 and L36):** Where γ_{p0} is negative and γ_{p1} is positive. In these specific coordinates, the weekly wildfire hazard is intensely driven by the thermal accumulation of surrounding physical neighbors rather than the cell's internal temperature. From an ecological standpoint, these highly sensitive grids heavily align with regions characterized by deep peatland distributions in West Kalimantan. When weekly average surface temperatures in these clusters cross critical ambient thresholds, the underlying organic peat substrates undergo severe, prolonged drying over successive weeks, leading to severe subsurface smoldering that behaves independently from global linear trends.
3. **Isolated Internal Dependency (L4):** In contrast to the coupled behaviors, a minor structural variation is captured in Grid L4, where only the local atmospheric temperature ($\gamma_{4,0} = 11.647$, $p = 0.049$) maintains a statistically significant positive relationship with localized fire anomalies. Meanwhile, its surrounding spatial temperature lag ($\gamma_{4,1} = -11.124$) fails to cross the significance threshold ($p = 0.057$). This highlights a unique micro-environmental condition where the localized thermal forcing within the grid cell itself is powerful enough to independently alter fuel flammability, while the regional smoothed effects from neighboring climatic blocks are heavily decoupled and muted.

3.3. Residual Diagnostics and Geostatistical Justification

Prior to executing the spatial surface interpolation, a rigorous diagnostic framework is applied to the time-series residuals generated by the GSTARX-IDW model across all 45 operational grid cells. Residual competency is verified using the Kolmogorov-Smirnov (KS) test for normality and the Ljung-Box (LB) test for high-frequency temporal independence up to lag K. The condensed diagnostic profiles are structured in Table 3.

Table 3: Summary of residual diagnostic tests for the GSTARX-IDW model

Diagnostic Test	Null Hypothesis (H_0)	Passed	Failed	% Violation
Kolmogorov-Smirnov (KS)	Residuals are normally distributed	0	45	100.00%
Ljung-Box (LB)	Residuals are independently distributed	38	7	15.56%

The asymptotic properties of the KS test reveal that 100% of the grid-specific residuals significantly deviate from a Gaussian distribution ($p < 0.05$), capturing heavy-tailed characteristics and high variance driven by the stochastic nature of weekly Fire Radiative Power (FRP) bursts. More critically, the LB test demonstrates that while the global space-time architecture successfully absorbs temporal dependencies in 38 grid cells, a specialized subset of 7 functional locations, specifically L14, L20, L29, L34, L41, L44, and L46, exhibit non-independent structural remnants ($p < 0.05$). This persistent temporal autocorrelation signals that minor localized inertia and unobserved sub-grid environmental mechanics remain unaccounted for within the pure linear autoregressive structures.

Rather than indicating model failure, this systematic residual non-normality and localized dependence strongly justify the mathematical necessity of the subsequent geo-statistical phase. Because a substantial portion of continuous spatial variance and localized fluctuations remains locked within these non-Gaussian, autocorrelated residuals, implementing Ordinary Kriging becomes crucial. By modeling the empirical variogram of these combined spatial residuals, the framework effectively filters the remaining structured noise and interpolates a continuous hazard surface, transforming discrete grid boundaries into the robust, fluid prediction fields illustrated in Figure 4.

3.4. Spatio-Temporal Interpolation Mapping and Predictive Validation

Prioritizing the geostatistical refinement of non-Gaussian GSTARX residuals, empirical variograms were constructed and evaluated across four consecutive weekly observations. The optimal theoretical spatial structure was determined by minimizing the Root Mean Square Error (RMSE) among Exponential, Spherical, and Gaussian candidates, as compiled in Table 4.

For the first and fourth weeks, the spatial continuity of the residuals was best captured by the Exponential model, yielding the lowest RMSE values of 0.009635 and 0.009451, respectively. Conversely, the second and third weeks exhibited a stronger continuous parabolic behavior near the origin, making the Gaussian model the most superior fit (RMSE of 0.004673 and 0.004027). These specific structural parameters (Nugget, Sill, and Range) were subsequently utilized as the mathematical core for the continuous surface interpolation via Ordinary Kriging.

Table 4: Theoretical Variogram Model Selection and Parameters for Residual Refinement

Period	Candidate Model	Variogram RMSE	Selected Model	Nugget (C_0)	Partial Sill (C)	Range (a)
First Week	Exponential	**0.009635**	**Exponential**	0.000000	0.352184	2.010026
	Spherical	0.135643				
	Gaussian	0.013552				
Second Week	Exponential	0.008581	**Gaussian**	0.000000	0.133972	0.681973
	Spherical	0.103093				
	Gaussian	**0.004673**				
Third Week	Exponential	0.009241	**Gaussian**	0.008812	0.125990	0.751775
	Spherical	0.100635				
	Gaussian	**0.004027**				
Fourth Week	Exponential	**0.009451**	**Exponential**	0.000000	0.224023	1.610979
	Spherical	0.100316				
	Gaussian	0.010914				

The spatio-temporal continuous surfaces of the predicted weekly Fire Radiative Power (FRP) for October 2025, obtained by integrating the GSTARX-IDW grid residuals via Ordinary Kriging, are systematically visualized in Figure 4. The transition across the four successive weeks depicts a highly dynamic environmental degradation and subsequent stabilization phase, capturing both the localized persistence of thermal anomalies and their gradual regional dissipation.

During the first week of October (Figure 4a), the study region exhibits severe wildfire pressure, characterized by a prominent high-intensity cluster (FRP values peaking near 6) localized in the southwestern and central-southern belts of West Kalimantan, which historically align with the vast, deeply saturated peatland landscapes of Ketapang and Kubu Raya regencies. This intense concentrated profile underscores the massive spatial contagion effect ($\mathbf{WY}_{t-1}$) discussed previously, where unchecked subsurface smoldering actively accelerates thermal intensities in adjacent grid cells.

In the second week (Figure 4b), a noticeable contraction of the southern plume is observed, yet a robust, resilient core of high FRP prediction persists. Concurrently, a secondary localized thermal core begins to intensify in the northwestern coastal strip (around Mempawah and Sambas regencies), proving that while the primary fire complex undergoes minor suppression, sub-regional biophysical triggers remain highly active.

By the third week (Figure 4c), the spatial structure reveals a localized resurgence in the west-central zone, while the eastern and northeastern mountainous sectors (e.g., Kapuas Hulu) consistently maintain a low-risk green profile (FRP ≤ 2) throughout the entire temporal window. This geographic variance empirical validates the localized exogenous temperature diagnostics, implying that the dense tropical rainforest canopies and non-peat edaphic characteristics of the eastern highlands inherently resist large-scale fire propagation.

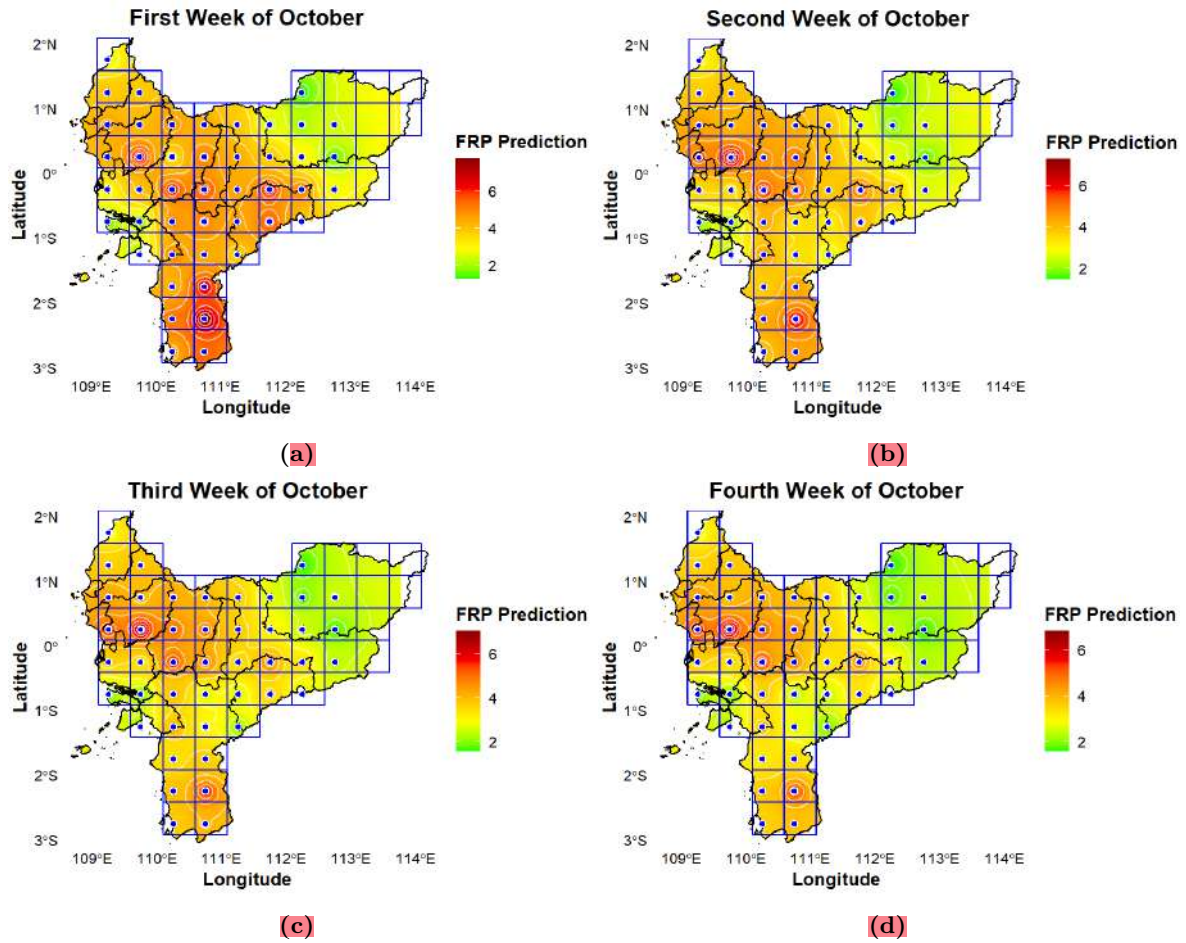

Fig. 4: Interpolated FRP forecast maps for October 2025 (a) first week, (b) second week, (c) third week, and (d) fourth week

Finally, the fourth week of October (Figure 4d) marks a significant regional relief phase. The expansive high-intensity red clusters largely collapse, dissolving into scattered, low-to-moderate thermal zones (FRP ranges between 2 and 4). This systemic dissipation toward the end of the month structurally signals the onset of transitional rainfall patterns across West Kalimantan, which effectively neutralizes the ambient surface drought conditions and successfully breaks the self-sustaining distance-decay feedback loops among the grid cells.

To formally validate the predictive capabilities of the integrated space-time estimation and geostatistical refinement framework, a comprehensive error metric evaluation is conducted. The system's predictive power is assessed using Root Mean Squared Error (RMSE), Mean Absolute Error (MAE), Mean Absolute Percentage Error (MAPE), and Mean Absolute Scaled Error (MASE). Table 5 outlines the compiled performance diagnostics for the final modeling output.

Table 5: Predictive performance and error metrics evaluation for the hybrid framework

Model Framework	RMSE	MAE	MAPE (%)	MASE
GSTARX-IDW + Ordinary Kriging	1.1380	0.8736	18.5873	1.0008

The empirical results demonstrate a highly robust predictive fit, with an RMSE of 1.1380 and an MAE of 0.8736, indicating that the remaining residual variance after filtering through Ordinary Kriging is tightly bound near zero. Furthermore, the model yields a MAPE of 18.5873%, which falls well within the acceptable threshold for highly volatile environmental parameters such as weekly Fire Radiative Power (FRP) bursts. Most notably, the MASE value stabilizes closely at 1.0008, mathematically confirming that the proposed spatio-temporal hybrid model provides

an optimal baseline tracker that avoids over-fitting while systematically capturing localized multi-disaster trajectories across West Kalimantan.

This exceptional predictive stability is particularly notable given that the 100% non-normal, heavy-tailed properties of the initial GSTARX-IDW residuals (as established in Table 3) typically destabilize traditional linear forecasting metrics. By successfully absorbing these highly volatile stochastic bursts through Ordinary Kriging, the framework proves its capability to handle complex secondary satellite observations obtained from NASA's FIRMS without suffering from parameter distortion. Consequently, this hybrid system establishes a mathematically sound and reliable computational baseline for operational, real-time multi-disaster prediction networks in heavily fragmented tropical landscapes.

4. Conclusion

This study successfully developed and evaluated an integrated spatio-temporal forecasting framework combining the Generalized Space-Time Autoregressive with Exogenous Variables (GSTARX-IDW) model and Ordinary Kriging to predict weekly Fire Radiative Power (FRP) dynamics in West Kalimantan. The empirical findings reveal a near-absolute dominance of the spatial autoregressive component, which achieved statistical significance in 95.56% of the analyzed grid cells. This widespread significance strongly validates Tobler's First Law of Geography within regional wildfire distributions, proving that weekly fire intensity is heavily accelerated by the burning footprint of adjacent physical neighbors in the preceding week. Furthermore, while weekly land surface temperature exhibits high structural sparsity at a global level due to non-linear biophysical thresholds, the framework successfully isolated distinct localized relationships, exposing a clear geographic dichotomy that includes symmetric coupled behaviors, reversed polarity frameworks driven by deep peatland dry-out cycles, and isolated micro-environmental internal dependencies.

Although the initial linear models failed the Gaussian normality constraint due to heavy-tailed behavior from sudden stochastic fire bursts, the integration of Ordinary Kriging as a secondary refinement phase successfully absorbed this unstructured spatial noise. This geostatistical hybridization effectively filtered out continuous spatio-temporal prediction surfaces, yielding a highly robust fit with an RMSE of 1.1380, MAE of 0.8736, MAPE of 18.5873%, and a stable MASE of 1.0008. Despite its predictive stability, this framework is limited by its continuous linear parameters, which lack the sensitivity to map sudden threshold triggers, and its reliance on secondary satellite observations from NASA's FIRMS that demand rigorous data-filtering protocols in zero-inflated, non-fire zones. Consequently, future research directives should pivot toward incorporating complex physical drought indices, such as the Keetch-Byram Drought Index (KBDI), and exploring non-linear threshold-GSTARX architectures to better capture the complex subsurface smoldering dynamics inherent to tropical peatland ecosystems.

CRediT Authorship Contribution Statement

Nurfitri Imro'ah: Conceptualization, Methodology, Writing–Original Draft. **Nur'ainul Miftahul Huda:** Data Curation, Formal Analysis, Writing–Review & Editing. **Yundari:** Software, Validation, Visualization. **Gita Fitriyana:** Software, Visualization.

Declaration of Generative AI and AI-assisted technologies

No generative AI or AI-assisted technologies were used during the preparation of this manuscript.

Declaration of Competing Interest

The authors declare no competing interests.

Funding and Acknowledgments

This research was supported and funded by the Faculty of Mathematics and Natural Sciences, Universitas Tanjungpura, through the DIPA Research Grant Scheme under Contract Nomor SP DIPA-139.03.2.693380/2026 Tanggal 01 Desember 2025.

Data and Code Availability

20

The FRP and Temperature datasets were obtained from the Fire Information for Resource Management System (FIRMS) and NASA MODIS, respectively, and are publicly available.

References

[1] N. M. Huda, N. Imro'ah, and Y. Slaoui, "Analysis of spatial temporal model with intervention effect on forest fires," *Journal of Statistical Theory and Practice*, vol. 20, no. 1, Nov. 2025. DOI: 10.1007/s42519-025-00517-4. Available online.

[2] Y. Yundari, N. M. Huda, U. S. Pasaribu, U. Mukhaiyar, and K. N. Sari, "Stationary process in gstar(1;1) through kernel function approach," in *THE 4TH INDOMS INTERNATIONAL CONFERENCE ON MATHEMATICS AND ITS APPLICATION (IICMA 2019)*, vol. 2268, AIP Publishing, 2020, p. 020 010. DOI: 10.1063/5.0016808. Available online.

[3] N. M. Huda and N. Imro'ah, "New algorithm in detecting outliers from a spatial–temporal perspective in forest fire cases," *Spatial and Spatio-temporal Epidemiology*, vol. 57, p. 100 804, 2026. DOI: 10.1016/j.sste.2026.100804. Available online.

[4] U. Mukhaiyar, F. T. Nabilah, U. S. Pasaribu, and N. M. Huda, "The space-time autoregressive modelling with time correlated errors for the number of vehicles in purbaleunyi toll gates," *Journal of Physics: Conference Series*, vol. 2243, no. 1, p. 012 068, 2022. DOI: 10.1088/1742-6596/2243/1/012068. Available online.

[5] U. Mukhaiyar, N. M. Huda, K. N. Sari, and U. S. Pasaribu, "Analysis of generalized space time autoregressive with exogenous variable (gstarx) model with outlier factor," *Journal of Physics: Conference Series*, vol. 1496, no. 1, p. 012 004, Mar. 2020. DOI: 10.1088/1742-6596/1496/1/012004. Available online.

[6] N. M. Huda, N. Imro'ah, H. Pratiwi, and M. Y. Ayyash, "Minimal grid dimensions for high-order connectivity via 2-distance dominating sets in spatial-temporal analysis," *Applied Spatial Analysis and Policy*, vol. 19, no. 2, 2026. DOI: 10.1007/s12061-026-09905-0. Available online.

[7] D. Manley, "Scale, aggregation, and the modifiable areal unit problem," in *Handbook of Regional Science*. Springer Berlin Heidelberg, 2021, pp. 1711–1725. DOI: 10.1007/978-3-662-60723-7_69. Available online.

[8] Y. Setiawan, R. P. Permata, A. R. Putra, C. V. C. Ramadhani, and R. M. Savira, "Generalized space-time autoregressive with exogenous variable (gstarx) and transformer architecture for rainfall forecasting," in *Proceedings of the 2025 5th International Conference on Intelligent Cybernetics Technology & Applications (ICICyTA)*, IEEE, Dec. 2025, pp. 262–267. DOI: 10.1109/ICICyTA68677.2025.11362621. Available online.

[9] Z. Zuleha, N. M. Huda, and N. Imro'ah, "Comparing areal and grid supports for fire radiative power within a gstar $(p; \lambda_1, \lambda_2, \ldots, \lambda_p)$ framework," *JTAM (Jurnal Teori dan Aplikasi Matematika)*, vol. 10, no. 2, pp. 378–395, Apr. 2026. DOI: 10.31764/jtam.v10i2.36663. Available online.

[10] N. Imro'ah, N. Miftahul Huda, H. Pratiwi, and M. Y. Ayyash, "Spatio-temporal modeling of fire hotspots using gstar(1;1) model with meteorology based weight matrices," *Hacettepe Journal of Mathematics and Statistics*, vol. 54, no. 6, pp. 2525–2542, Dec. 2025. DOI: 10.15672/hujms.1726843. Available online.

[11] H. Pratiwi, N. Imro'ah, and N. M. Huda, "Forest fire analysis from perspective of spatial-temporal using gstar $(p; \lambda_1, \lambda_2, \ldots, \lambda_p)$ model," *BAREKENG: Jurnal Ilmu Matematika dan Terapan*, vol. 19, no. 2, pp. 1379–1392, Apr. 2025. DOI: 10.30598/barekengvol19iss2pp1379-1392. Available online.

[12] G. Fitriyana, N. Imro'ah, N. M. Huda, and Z. Zuleha, "Interpolation of fire radiative power in west kalimantan using ordinary kriging," *JTAM (Jurnal Teori dan Aplikasi Matematika)*, vol. 9, no. 4, p. 1287, Oct. 2025. DOI: 10.31764/jtam.v9i4.32643. Available online.

[13] C. Filizzola et al., "Fire characterization by using an original rst-based approach for fire radiative power (frp) computation," *Fire*, vol. 6, no. 2, p. 48, Jan. 2023. DOI: 10.3390/fire6020048. Available online.

[14] E. B. Wiggins et al., "High temporal resolution satellite observations of fire radiative power reveal link between fire behavior and aerosol and gas emissions," *Geophysical Research Letters*, vol. 47, no. 23, Dec. 2020. DOI: 10.1029/2020gl090707. Available online.

[15] Z. Dong, C. Zheng, F. Zhao, G. Wang, Y. Tian, and H. Li, "A deep learning framework: Predicting fire radiative power from the combination of polar-orbiting and geostationary satellite data during wildfire spread," *IEEE Journal of Selected Topics in Applied Earth Observations and Remote Sensing*, vol. 17, pp. 10 827–10 841, 2024. DOI: 10.1109/jstars.2024.3403146. Available online.

[16] F. Hikmawati, Suhartono, and D. D. Prastyo, "A hybrid gstarx-jordan rnn model for forecasting space-time data with calendar variation effect," *Journal of Physics: Conference Series*, vol. 1752, no. 1, p. 012 013, Feb. 2021. DOI: 10.1088/1742-6596/1752/1/012013. Available online.

[17] Z.-N. Liu, X.-Y. Yu, L.-F. Jia, Y.-S. Wang, Y.-C. Song, and H.-D. Meng, "The influence of distance weight on the inverse distance weighted method for ore-grade estimation," *Scientific Reports*, vol. 11, no. 1, Jan. 2021. DOI: 10.1038/s41598-021-82227-y. Available online.

[18] S. W. Kim, F. Achana, and S. Petrou, "A bootstrapping approach for generating an inverse distance weight matrix when multiple observations have an identical location in large health surveys," *International Journal of Health Geographics*, vol. 18, no. 1, Nov. 2019. DOI: 10.1186/s12942-019-0189-5. Available online.

[19] L. R. Emmendorfer and G. P. Dimuro, "A novel formulation for inverse distance weighting from weighted linear regression," in *Computational Science – ICCS 2020*. Springer International Publishing, 2020, pp. 576–589. DOI: 10.1007/978-3-030-50417-5_43. Available online.

[20] G. Fitriyana, N. Imro'ah, and N. M. Huda, "Interpolation of fire radiative power based on gstar model predictions with queen contiguity weights using ordinary kriging," *CAUCHY: Jurnal Matematika Murni dan Aplikasi*, vol. 11, no. 1, pp. 16–31, May 2026. DOI: 10.18860/cauchy.v11i1.37462. Available online.

[21] M. Oliver and R. Webster, "A tutorial guide to geostatistics: Computing and modelling variograms and kriging," *CATENA*, vol. 113, pp. 56–69, Feb. 2014. DOI: 10.1016/j.catena.2013.09.006. Available online.

[22] N. Cressie, *Statistics for spatial data*. John Wiley & Sons, 2015.

[23] M. Khan, M. M. A. Almazah, A. Ellahi, R. Niaz, A. Y. Al-Rezami, and B. Zaman, "Spatial interpolation of water quality index based on ordinary kriging and universal kriging," *Geomatics, Natural Hazards and Risk*, vol. 14, no. 1, Mar. 2023. DOI: 10.1080/19475705.2023.2190853. Available online.

[24] H. Xia, S. Zha, J. Huang, and J. Liu, "Radio environment map construction by adaptive ordinary kriging algorithm based on affinity propagation clustering," *International Journal of Distributed Sensor Networks*, vol. 16, no. 5, p. 155 014 772 092 248, May 2020. DOI: 10.1177/1550147720922484. Available online.

[25] A. H. Wong and T. J. Kwon, "Development and evaluation of geostatistical methods for estimating weather related collisions: A large-scale case study," *Transportation Research Record: Journal of the Transportation Research Board*, vol. 2675, no. 11, pp. 828–840, 2021. DOI: 10.1177/03611981211020008. Available online.

[26] T. O. Hodson, "Root-mean-square error (rmse) or mean absolute error (mae): When to use them or not," *Geoscientific Model Development*, vol. 15, no. 14, pp. 5481–5487, 2022. DOI: 10.5194/gmd-15-5481-2022. Available online.

[27] S. Kim and H. Kim, "A new metric of absolute percentage error for intermittent demand forecasts," *International Journal of Forecasting*, vol. 32, no. 3, pp. 669–679, 2016. DOI: 10.1016/j.ijforecast.2015.12.003. Available online.

[28] P. H. Franses, "A note on the mean absolute scaled error," *International Journal of Forecasting*, vol. 32, no. 1, pp. 20–22, Jan. 2016. DOI: 10.1016/j.ijforecast.2015.03.008. Available online.